Monthly Notices of the ROYAL ASTRONOMICAL SOCIETY

MNRAS **513,** 886–899 (2022) https://doi.org/10.1093/mnras/stac865
Advance Access publication 2022 March 31

# IGR J18249−3243: a new GeV-emitting FR II and the emerging population of high-energy radio galaxies

G. Bruni [1]★ L. Bassani,[2] M. Persic [3,4] Y. Rephaeli,[5,6] A. Malizia,[2] M. Molina [7] M. Fiocchi [1] R. Ricci,[8] M. H. Wieringa,[9] M. Giroletti [8] F. Panessa [1] A. Bazzano[1] and P. Ubertini[1]

[1]*INAF – Istituto di Astrofisica e Planetologia Spaziali, via Fosso del Cavaliere 100, I-00133 Roma, Italy*
[2]*INAF – Osservatorio di Astrofisica e Scienza dello Spazio, via P. Gobetti 101, I-40129 Bologna, Italy*
[3]*INAF – Osservatorio Astronomico di Trieste, via G.B. Tiepolo 11, I-34100 Trieste, Italy*
[4]*INFN – Trieste, via A. Valerio 2, I-34127 Trieste, Italy*
[5]*School of Physics and Astronomy, Tel Aviv University, Tel Aviv 69978, Israel*
[6]*Center for Astrophysics and Space Sciences, University of California at San Diego, La Jolla, CA 92093, USA*
[7]*INAF – Istituto di Astrofisica Spaziale e Fisica Cosmica, Via A. Corti 12, I-20133 Milano, Italy*
[8]*INAF – Istituto di Radioastronomia, via P. Gobetti 101, I-40129 Bologna, Italy*
[9]*CSIRO – Astronomy and Space Science, PO Box 76, Epping, New South Wales 1710, Australia*

Accepted 2022 March 22. Received 2022 March 18; in original form 2022 January 28

## ABSTRACT

The advent of new all-sky radio surveys such as the VLA Sky Survey and the Rapid ASKAP Continuum Survey, performed with the latest generation radio telescopes, is opening new possibilities on the classification and study of extragalactic $\gamma$-ray sources, specially the underrepresented ones like radio galaxies. In particular, the enhanced sensitivity (sub-mJy level) and resolution (a few arcsec) provides a better morphological and spectral classification. In this work, we present the reclassification of a *Fermi*/Large Area Telescope (LAT) source as a new Fanaroff–Riley II radio galaxy from the International Gamma-Ray Astrophysics Laboratory sample found to emit at GeV energies. Through a broad-band spectral fitting from radio to $\gamma$-ray, we find that the commonly invoked jet contribution is not sufficient to account for the observed $\gamma$-ray flux. Our modelling suggests that the observed emission could mainly originate in the lobes (rather than in the radio core) by inverse Compton scattering of radio-emitting electrons off the ambient photon fields. In addition, we cross-correlated the latest generation radio surveys with a list of *Fermi*/LAT candidate misaligned AGN from the literature, finding four new radio galaxies with a double-lobed morphology. Additional four objects could be classified as such thanks to previous studies in the literature, for a total of nine new radio galaxies with GeV emission presented in this work. We foresee that further objects of this class might be found in the near future with the advent of the Square Kilometer Array, populating the GeV sky.

**Key words:** galaxies: individual: IGR J18249−3243 – galaxies: individual: IGR J13109−5552 – galaxies: jets – gamma-rays: galaxies – radio continuum: galaxies.

## 1 INTRODUCTION

The $\gamma$-ray sky in the GeV energy range is dominated by active galactic nuclei (AGNs), as revealed in the past years by the *Fermi*/Large Area Telescope (LAT). Most of the AGNs detected in $\gamma$-rays are blazars, namely radio-loud AGNs whose jets are oriented close to our line of sight (i.e. $\leq 10$ deg). In the fourth *Fermi* AGN catalogue (4LACl; Ajello et al. 2020) 98% of the detected objects are blazars, while the remainder 2% are other types of AGNs, collectively named non-blazar sources. These are 69 objects divided into 41 radio galaxies, 9 Narrow Line Seyfert 1 galaxies, 5 Compact Steep Spectrum radio sources, 2 steep-spectrum radio quasar, 1 Seyfert galaxy, and 11 AGNs, whose specific class is still unclear (Ajello et al. 2020). These object types are of particular interest, since they can provide information on the role of jets in non-blazar objects.

Among *Fermi* non-blazar AGN, radio galaxies constitute the dominant class and are particularly interesting since they are considered appealing laboratories to study the high-energy processes at play in AGNs (see e.g. Grandi, Torresi & Stanghellini 2012; Torresi et al. 2018). Indeed, their broad-band spectral energy distribution shows signatures of both accretion and jet-related emission. In particular, while the radio and $\gamma$-ray emission is likely due to a jet, the infrared-to-X-ray continuum is generally found to be dominated by the thermal radiation from accreting matter, such as the accretion disc and the hot X-ray-emitting corona (e.g. Wozniak et al. 1998; Grandi & Palumbo 2007; Kataoka et al. 2011). Furthermore, they provide a test bed where jet progressive misalignment can be studied and analysed. Radio galaxies or misaligned blazar can also be found among still unidentified $\gamma$-ray AGN or between objects wrongly classified as blazars.

For the two nearby and very extended sources Centaurus A and Fornax A (angular size $\gtrsim 1$ deg), *Fermi*/LAT was able to detect $\gamma$-ray emission associated with the lobes (Abdo et al. 2010a; Ackermann

★ E-mail: gabriele.bruni@inaf.it

et al. 2016). This allowed, for the first time, to spatially resolve the emission coming from the lobes and the core even in the GeV domain. Interestingly, the core contribution to the total $\gamma$-ray flux was found to be <14 per cent in Fornax A (Ackermann et al. 2016). A thorough spectral energy distribution (SED) modelling of the lobes emission in the radio and $\gamma$-rays (McKinley et al. 2015; Ackermann et al. 2016) concluded that both leptonic and hadronic models can explain the observational properties, with a combination of the two being the most probable explanation for the case of Fornax A. Nevertheless, this would imply a high-energy density for protons, or filaments with a high gas density and magnetic field energy (McKinley et al. 2015). Recent studies reconsidered the leptonic model, demonstrating how inverse Compton of the radio-emitting electrons off the ambient optical radiation field can be sufficient to account for the GeV emission in a set of four radio galaxies (Persic & Rephaeli 2019a,b, 2020).

We present here a newly discovered radio galaxy, namely IGR J18249−3243, which belongs to the complete sample of AGN detected by the International Gamma-Ray Astrophysics Laboratory (*INTEGRAL*) with the Imager on Board the INTEGRAL Satellite (IBIS) detector in its first years of survey (Malizia et al. 2009). It is associated with PKS 1821−327 that has been classified as AGN of unknown type in the fourth *Fermi* Large Area Telescope catalogue (4FGL; Abdollahi et al. 2020). In this work, we discuss its properties thanks to recently acquired radio data, and how the GeV $\gamma$-ray emission might be mostly produced in the lobes. During the same campaign, we collected data for another *INTEGRAL*/IBIS source missing a definitive classification (IGR J13109−5552), that we could reveal to be a blazar (see Appendix B). In addition, we present a list of new radio galaxies showing GeV emission in the 4FGL catalogue, whose classification was possible thanks to images from the latest radio surveys.

In this work-, we adopt the standard cosmological parameters $H_0 = 71$ km s$^{-1}$Mpc$^{-1}$, $\Omega = 0.27$, $\Omega_\Lambda = 0.73$, analogously to our previous works (Bassani et al. 2016), and the convention $S \propto \nu^{\alpha}$ for the spectral index definition.

## 2 THE RADIO GALAXY IGR J18249−3243

IGR J18249−3243 was first detected by *INTEGRAL*/IBIS and reported as a new AGN by Bassani et al. (2016) who tentatively associated it with the poorly studied radio source PKS 1821−327. The X-ray counterpart measured by *Swift*/X-ray Telescope (XRT), needed to confirm this radio association and to provide an optical classification throughout follow-up observations, was reported by Landi et al. (2007). The X-ray core is located at RA(J2000) = 18:24:56.11, Dec(J2000) = –32:42:58.9 with a positional uncertainty of 3.7 arcsec and thus is around 15–20 arsec away from the radio source position (depending on the radio catalogue used). In due course, Masetti et al. (2009) observed the optical counterpart of IGR J18249−3243 with the 1.5 m at the Cerro Tololo Interamerican Observatory (CTIO) in Chile, providing for the first time the source redshift ($z = 0.355$), optical spectrum and AGN class (Seyfert 1, showing broad emission lines). At the same time, Landi et al. (2009) explored the broad-band characteristics of the system (from radio to X-rays) finding that the source is radio loud, has a complex radio morphology and a steep radio spectrum, while confirming at the same time the AGN nature of the system. By using the combined X-ray Multi-Mirror Mission (*XMM*)/pn–*INTEGRAL*/IBIS spectrum, Malizia et al. (2014) further explored the high-energy properties of the source finding that a simple power law ($\Gamma = 2$), with no evidence for a high-energy cut-off, well describes the source spectrum from 0.2 to 200 keV.

So far, IGR J18249−3243 has never been reported as a *Swift*/Burst Alert Telescope (BAT) source, probably due to its location on the galactic plane where the *INTEGRAL*/IBIS coverage is much deeper. The most recent update on this source is its detection as a $\gamma$-ray emitter, since it is now listed in 4LAC as a non-blazar object (Ajello et al. 2020). The GeV $\gamma$-ray spectrum can be described by a simple power law with photon index $2.227 \pm 0.122$ and a 0.1–100 GeV flux of $3.8 \pm 0.81 \times 10^{-12}$ erg cm$^{-2}$ s$^{-1}$. The $\gamma$-ray photon index and luminosity ($1.6 \times 10^{45}$ erg s$^{-1}$) locate the galaxy in a region of the ($L_\gamma$, $\Gamma$) diagram mostly populated by blazars (see fig. 11 in Ajello et al. 2020). Since the optical spectrum of the source shows emission lines, the most likely association would be with a flat spectrum radio quasar; however, the steep radio spectral index, as estimated from surveys (see next section), is not compatible with this classification. Before this work, no radio image has been able to fully resolve its structure nor the source has been studied in some details to allow a more specific characterization of its radio components.

### 2.1 Radio characterization

The source was in the footprint of several surveys in the radio band, among which the NRAO VLA sky Survey (NVSS; Condon et al. 1998, 1.4 GHz), the Parkes-MIT-NRAO survey (PMN; Griffith & Wright 1993, 4.8 GHz), the Galactic and extragalactic all-sky MWA survey (GLEAM; Wayth et al. 2015, 74–231 MHz), and in the TIFR GMRT Sky Survey (TGSS; Intema et al. 2017, 150 MHz). However, none of these were able to fully resolve the source morphology. The NVSS image, at a resolution of 45 arcsec, shows a single component with an elongation towards West. Its total flux density is $4080 \pm 204$ mJy, resulting in a radio power of $1.26 \times 10^{27}$ W/Hz. The TGSS, at a slightly higher resolution of 41 arcsec × 25 arcsec, better resolves the elongated structure showing an enhanced flux density on the Eastern side. A projected linear size of about 2 arcmin can be estimated. The overall spectral index, considering the flux densities from NVSS and PMN, is steep (–0.77).

Lately, with the advent of new generation radio telescopes, more sensitive and accurate surveys are scanning the sky: the VLA Sky Survey (VLASS, Lacy et al. 2020), and the Rapid ASKAP Continuum Survey (RACS, McConnell et al. 2020). The angular resolution is ∼2.5 arcsec for VLASS, while ∼15 arcsec for RACS. The sensitivity is at a similar sub-mJy level of ∼0.12 mJy per beam for the first epoch of VLASS, and ∼0.25 mJy per beam for RACS. However, thanks to the lower frequency and shorter minimum baseline, RACS can detect larger structures than VLASS: the largest angular scale visible by VLASS is ∼1 arcmin, versus ∼1 deg for RACS. Together, they provide a full coverage of the sky. We browsed the first epoch of VLASS quick look images[1] and found that the angular resolution is sufficient to disclose the morphology of IGR J18249−3243. In Fig. 1, the source is resolved into three radio components, which all together present the typical morphology of a radio galaxy, with a central core and two lobes. The central component is located within the positional uncertainty of the X-ray coordinates from *Swift*/XRT (pink, dashed circle in Fig. 1), thus consistent with the core. The total angular scale of the source, as measured between lobes extremities, is 64 arcsec, corresponding to 317 kpc at the source redshift. The surface brightness, larger

[1] https://science.nrao.edu/vlass/data-access/vlass-epoch-1-quick-look-users-guide

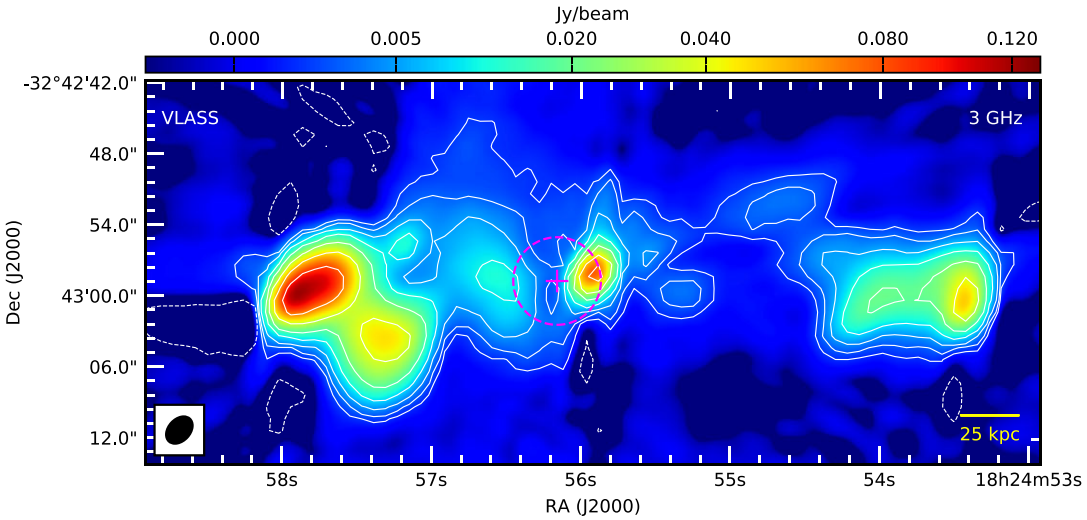


**Figure 1.** VLASS image of IGR J18249−3243. The cross and the dashed circle indicate the position of the X-ray core as measured by *Swift*/XRT, with the corresponding uncertainty. The contours are multiple of the image rms, namely 3 × rms × (−1, 1, 2, 4, 8, 16, 32, 64). The rms is 0.411 mJy per beam. The beam is reported in the lower left corner.

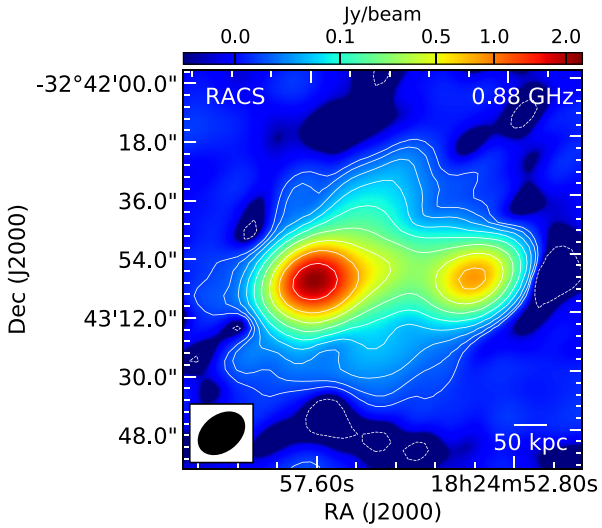


**Figure 2.** RACS image of IGR J18249−3243 at 0.88 GHz. The contours are multiple of the image rms, namely 3 × rms × (−1, 1, 2, 4, 8, 16, 32, 64, 128, 256). The RMS is 2.09 mJy per beam. The beam is reported in the lower left corner.

for the lobes and slightly dimmer for the core, is suggestive of the Fanaroff–Riley II (FR II) class. Indeed, the core flux density is 118 ± 12 mJy, while the Eastern (A) and Western (B) lobes show values of 942 ± 94 mJy and 333 ± 33 mJy, respectively. This results in a core dominance (CD, defined as $S_{\rm core}/(S_{\rm tot} - S_{\rm core})$) of 0.09. This value is among the lowest ones found for FR I or FR II radio galaxies previously detected by *Fermi*/LAT (Abdo et al. 2010b), suggesting a larger viewing angle. The RACS image at 0.8 GHz has a lower resolution (16 arcsec × 11arcsec), nevertheless it resolves the source in two extended components, corresponding with the two lobes (see Fig. 2). At the core position, as derived from the VLASS images, the emission is partly blended with the Eastern lobe. The better capability of the RACS to recover extended emission allows to detect two symmetric tails of emission, on the Northern and one on the Southern side, suggestive of deflected plasma backflow from the lobes (see e.g. Cotton et al. 2020).

### 2.1.1 *ATCA observations*

Given the resolved morphology revealed by VLASS, we targeted the source with Australian Telescope Compact Array (ATCA) on 2021 September 20. We performed a 5-h ATCA observing run as part of the project C3412 (PI: Ricci) at 5.5, 9, and 17 GHz. The array configuration was 6A, providing an angular resolution of 4.88 × 1.17 arcsec at 5.5 GHz, 2.93 × 0.83 at 9 GHz, and 3.02 × 0.42 at 17 GHz. The raw RPFITS files were read into MIRIAD, flagged for Radio Frequency Interferences (RFIs) and calibrated following the same scheme used for AT20G data. The bandpass calibrator was 0537 − 441, the primary calibrator 1934 − 638, and phase calibrator 1759 − 39. As the phases were still very unstable after the standard phase calibration because of atmospheric turbulence, three rounds of phase self-calibration were performed inside MIRIAD to improve phase stability and thus the restored image quality. Finally, images at 9 and 17 GHz were tapered and restored applying the same beam for the 5.5 GHz one, in order to restore the resolved emission from the lobes. The obtained images are shown in Fig. 3.

These observations, at a resolution and sensitivity similar to VLASS, could confirm the previously discussed morphology, and provide the frequency coverage necessary to study the spectral properties of the different components. Flux densities for the three components, together with information about the images collected from surveys, are presented in Table 1. We built a spectral energy distribution for the different components (see Fig. 4). We found spectral indices between 5.5 and 9 GHz as expected, i.e. steep for the lobes (–1.43 ± 0.14 for A, and –1.6 ± 0.14 for B) while flat for the core (–0.19 ± 0.15), considering a value of –0.5 as boundary between steep and flat spectra. Overall, the discussed radio and optical properties suggest that this source is seen at an intermediate angle between the plane of the sky and the jet axis, allowing to detect broad emission lines in the optical band, but also a symmetric morphology with VLASS and ATCA, typical of radio galaxies.

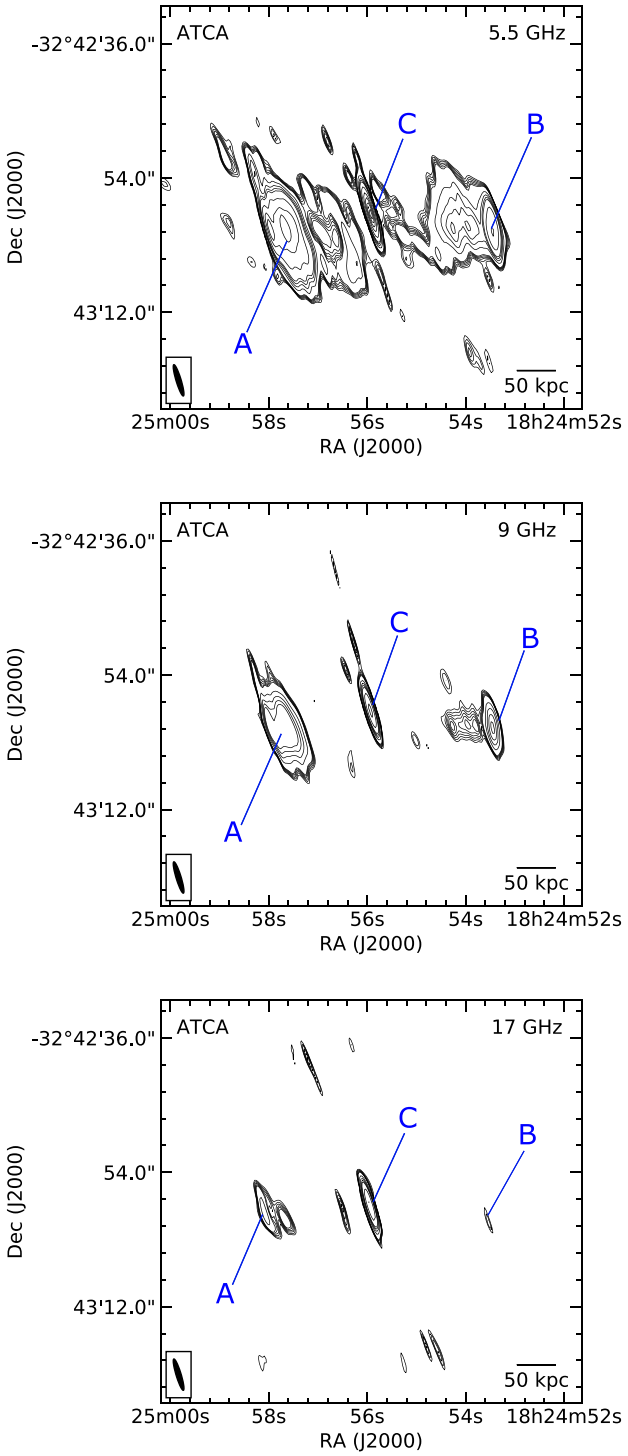


**Figure 3.** ATCA images of IGR J18249−3243 at 5, 9, and 17 GHz. The contours are multiple of the image rms, namely rms × (5, 6, 7, 8, 9, 10, 20, 30, 40, 50, 60, 70, 80, 90, 100, 200, 300, 400, 500). The rms is 0.21, 0.47, and 0.37 mJy per beam for the three frequencies, respectively. The beam is reported in the lower left corner.

### 2.2 Broad-band SED and the origin of the $\gamma$-ray emission

We performed an analysis of the broad-band SED, in order to understand which emission mechanisms dominate the different energy ranges. In addition to the radio data described in the previous section, we made use of *XMM*/pn data to cover the X-rays energy range, and the previously mentioned *INTEGRAL*/IBIS and *Fermi*/LAT survey data for the hard X-rays and $\gamma$-ray ones, respectively. The fluxes and upper limits from *Fermi*/LAT were cross-checked by inquiring the online version of the 4FGL catalogue on VizieR.[2] The source was not reported as variable in the latter. In addition, we browsed archival data with the ASI Science Data Center (ASDC) online tool[3] to cover the infrared (IR)/optical bands. However, photometry results to be contaminated by an intervening star, thus could not be used for our target SED. The collected fluxes are reported in Table 2.

#### *2.2.1 Thermal and non-thermal emission from the central AGN*

With these data at hand, we performed a broad-band SED fitting adopting the hybrid model approach by Kataoka et al. (2011). This is a phenomenological model for type 1 AGN, considering a thermal component accounting for the IR to hard X-rays emission produced by the accretion disc, corona, and dusty torus, and a non-thermal component describing the emission from the jet in the radio and $\gamma$-ray band. The purpose of such a simplistic modelling is limited to the quantification of the nuclear contribution to the overall SED, and in particular to verify whether the inner part of the jet can be at the origin of the $\gamma$-ray emission detected by *Fermi*/LAT. Templates available in the literature were considered for both components, namely the average SED for Seyfert 1 built by Prieto et al. (2010) for the thermal component, and the average 3C 273 SED from Soldi et al. (2008) for the non-thermal one. Analogously to Kataoka et al. (2011), we considered the 5 GHz radio flux densities from the core region only as a constraint for the 3C 273 template, since the blazar-like, non-thermal emission described by the 3C 273 template is dominated by the core. As for the Seyfert 1 template, the model should have been matched to the infrared-to-X-rays continuum. However, only the X-rays/hard X-rays ranges were covered by meaningful measurements, while the optical and NIR data points were not usable due to the previously mentioned contamination by an intervening star. Thus, we preferred not to use the thermal model for further analysis. The result is shown in Fig. 6.

The non-thermal component is found to be in good agreement with the ATCA and VLASS measurements. However, the three *Fermi*/LAT detections have a flux excess of about an order of magnitude with respect to the values expected from the template. This supposes an additional emission mechanism or region from what found by Kataoka et al. (2011) for X-ray bright broad-line radio galaxies, where the GeV emission was found to be dominated by the beamed radiation from the relativistic jet. Indeed, in their work the *Fermi*/LAT fluxes were in good agreement with the ones expected from the non-thermal component. We note that the source has a hard X-rays luminosity (14–195 keV) among the highest ones found for the combined *Swift*/BAT + *INTEGRAL*/IBIS radio galaxies sample (Bassani et al. 2016). This possibly indicates the need for an additional emitting component in the high-energy portion of the SED. However, because of the lack of reliable measurements in the near-IR (NIR)-to-optical range, the expected yield in the soft and hard X-ray

[2] https://vizier.cds.unistra.fr/viz-bin/VizieR
[3] http://tools.asdc.asi.it/

**Table 1.** Radio flux densities for the different components of IGR J18249−3243. A corresponds to the Eastern lobe, C to the core, and B to the Western lobe. For RACS, we give only the value for component B, because A and C are blended.

| Telescope | Frequency (GHz) | Bandwidth (GHz) | Resolution (arcsec) | Rms (mJy per beam) | Date (yyyy-mm-dd) | Component | Flux density (mJy) |
|---|---|---|---|---|---|---|---|
| RACS | 0.88 | 0.28 | 15.67 × 10.89 | 2.09 | 2019-04-28 | A | – |
| | | | | | | B | 913 ± 91 |
| | | | | | | C | – |
| VLASS | 3 | 2 | 2.61 × 1.85 | 0.37 | 2018-02-03 | A | 942 ± 94 |
| | | | | | | B | 333 ± 33 |
| | | | | | | C | 118 ± 12 |
| ATCA | 5.5 | 2 | 4.88 × 1.17 | 0.21 | 2021-09-30 | A | 603 ± 30 |
| | | | | | | B | 198 ± 10 |
| | | | | | | C | 122 ± 6 |
| ATCA | 9 | 2 | 4.88 × 1.17 | 0.47 | 2021-09-30 | A | 298 ± 15 |
| | | | | | | B | 90.3 ± 4.5 |
| | | | | | | C | 111 ± 6 |
| ATCA | 17 | 4 | 4.88 × 1.17 | 0.57 | 2021-09-30 | A | 32.4 ± 1.6 |
| | | | | | | B | 6.7 ± 0.3 |
| | | | | | | C | 78.4 ± 4.1 |

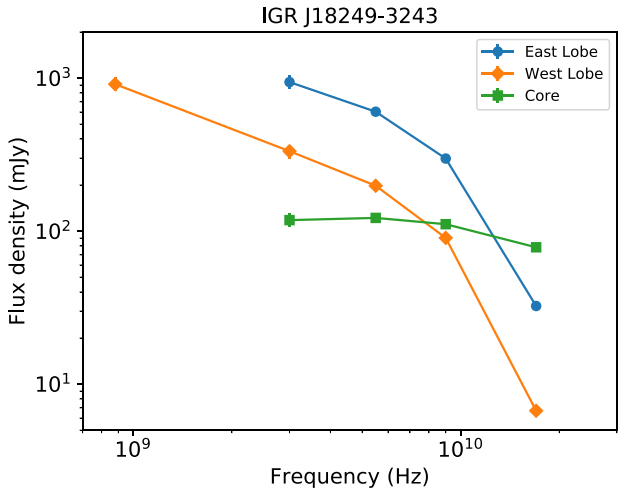


**Figure 4.** Radio SED for the lobes and core of IGR J18249–3243, built with data from VLASS (3 GHz), and ATCA data from our campaign (5.5, 9, and 17 GHz).

**Table 2.** High-energy data collected for the broad-band SED of IGR J18249−3243.

| Instrument | Band | Flux ($\times 10^{-13}$ erg cm$^{-2}$ s$^{-1}$) |
|---|---|---|
| *XMM*/pn | 0.2–0.5 (keV) | 1.55 ± 0.14 |
| | 0.5–1 | 6.53 ± 0.60 |
| | 1–2 | 13.0 ± 1.2 |
| | 2–4.5 | 22.1 ± 2.2 |
| | 4.5–12 | 37.2 ± 3.9 |
| *INTEGRAL*/IBIS | 20–40 (keV) | 39 –1/+4 |
| | 40–100 | <42 |
| *Fermi*/LAT | 0.05–0.1 (GeV) | <58.2 |
| | 0.1–0.3 | <10.9 |
| | 0.3–1 | 6.92 –3.44/+3.41 |
| | 1–3 | 6.95 –1.90/+1.94 |
| | 3–10 | 5.81 –1.73/+1.86 |
| | 10–30 | <2.13 |
| | 30–300 | <3.19 |

region cannot be predicted, and thus the presence of X-ray excess (with respect to the expected fluxes from the Seyfert 1 template) cannot be determined.

Finally, we note that previous studies on the radio/$\gamma$-ray connection in the *Fermi*/LAT AGN sample reported a considerable scatter of the GeV emission values for a given radio luminosity (Ackermann et al. 2011). That result, while establishing a significant correlation between the two quantities, allows for a wide range of luminosities to be expected for $\gamma$-ray counterparts of radio sources, thus mitigating the apparent $\gamma$-ray excess highlighted by the modelling approach proposed by Kataoka et al. (2011), and adopted in this work.

### 2.2.2 *Lobe $\gamma$-ray emission*

As discussed before, analysis of the SED indicates the need for an additional component of $\gamma$-ray emission, beyond that of the core, to account for the flux measured by *Fermi*/LAT. In accord with previous studies (Persic & Rephaeli 2019a), an appreciable contribution to the $\gamma$-ray emission could come from the radio lobes. Resolved radio maps and spectral X-ray and $\gamma$-ray measurements of the lobes of several radio galaxies have provided a basis for determining the emission processes, the spectrum of the energetic particles ('cosmic rays'), and the mean value of the magnetic field in the lobes. It has been shown that for a proper spectral analysis, the superposed radiation fields in the lobes need to be accounted for (Fornax A: Persic & Rephaeli 2019a; Centaurus A, Centaurus B, and NGC 6251: Persic & Rephaeli 2019b). These SED analyses have confirmed the leptonic lobe origin of the $\gamma$-ray emission measured by *Fermi*/LAT, thereby constraining the level of hadronic contribution to less than $\sim 10-20\%$.

Radio maps of IGR J18249−3243 show the presence of nuclear emission and two asymmetric but roughly comparable, off-centre emission regions whose centres are located at ∼120 kpc east and west of the central galaxy at a luminosity distance of 1.88 Gpc. Whereas most of the radio emission is in the lobes, X-ray emission is dominated by a central point-like source (see Fig. 5). However, diffuse emission beyond the *XMM* point spread function (PSF) cannot be excluded, although not visible in the *XMM* image. Future *Chandra* high spatial resolution images may allow us to provide an estimate on the flux in the lobes region. Neither the *INTEGRAL*/IBIS nor the *Fermi*/LAT emission is resolved.

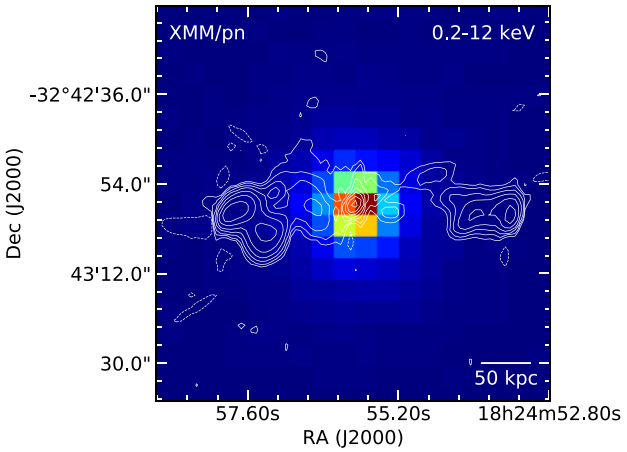


**Figure 5.** Overlay of the VLASS contours on the *XMM*/pn image (0.2–12 keV). The X-ray emission is dominated by a central point-like source corresponding with the radio core.

The radio emitting (cosmic ray) electrons (CRe) in the lobes and the central galaxy (jets, disc, and halo) emit also X/$\gamma$-ray by Compton scattering off the cosmic microwave background (CMB) and the local radiation field. Here, we model the diffuse non-thermal emission of IGR J18249−3243 following Persic & Rephaeli (2019a,b, 2020). A precise determination of the ambient photon fields in the lobes is needed to predict Compton X/$\gamma$-ray emission by CRe. Radiation fields in the lobes include cosmic and local components. Cosmic radiation fields include the CMB and the extragalactic background light (EBL). The CMB temperature is $T_{\rm CMB} = 2.725\,(1+z)$ K and energy density $u_{\rm CMB} = 0.25\,(1+z)^4$ eV cm$^{-3}$. The EBL originates from direct and dust-reprocessed starlight integrated over the star formation history of the Universe. Adopting a recent updated EBL model, based on galaxy counts in several spectral bands (Franceschini & Rodighiero 2017), at $z = 0.355$ the EBL photon number density can be numerically approximated as a combination of diluted Planckians,

$$n_{\rm EBL}(\epsilon) = \sum_{j=1}^{8} A_j \frac{8\pi}{h^3c^3} \frac{\epsilon^2}{e^{\epsilon/k_B T_j} - 1} \quad {\rm cm^{-3}\ erg^{-1}} \qquad (1)$$

with: $A_1 = 10^{-5.596}$, $T_1 = 31.522$ K; $A_2 = 10^{-7.231}$, $T_2 = 61.053$ K; $A_3 = 10^{-9.574}$, $T_3 = 207.143$ K; $A_4 = 10^{-11.629}$, $T_4 = 517.857$ K; $A_5 = 10^{-13.249}$, $T_5 = 2088$ K; $A_6 = 10^{-14.536}$, $T_6 = 4495$ K; $A_7 = 10^{-16.496}$, $T_7 = 10000$ K; $A_8 = 10^{-18.124}$, $T_8 = 23200$ K.

The local radiation fields (Galaxy Foreground Light, GFL) arise from the IR and optical humps of the central galaxy. Its bolometric optical luminosity is $L_{\rm opt} \sim 10^{46}$ erg s$^{-1}$, estimated from $V \simeq 15.86$ mag (Onken et al. 2019; however, this magnitude may be affected by a foreground star: Masetti et al. 2009) and applying the bolometric correction ${\rm BC}_V = -0.85$ (Buzzoni, Arnaboldi & Corradi 2006). The bolometric total IR (8–1000 μm) luminosity, $L_{\rm IR} \sim 4 \times 10^{45}$ erg s$^{-1}$, is estimated from $l_B$ (monochromatic blue luminosity, $l_B = L_B/6.88E + 14$ Hz) using the $L_{\rm FIR}$–$l_B$ relation by Trinchieri, Wolter & Iovino (1998) for late-type spirals (in the far-IR 60–100 μm, band), assuming $L_{\rm IR} \sim 1.7\,L_{\rm FIR}$ (Persic & Rephaeli 2007). However, given that the contribution of the scattered IR field to the LAT $\gamma$-ray data is very small, the actual value of $L_{\rm IR}$ is unimportant. The IR and optical parameters allow us to model the GFL; in our calculations we take $T_{\rm gal,\,OPT} = 2900$ K and $T_{\rm gal,\,IR} = 29$ K (Persic & Rephaeli 2019a). The lobe X-ray data are spatial averages, so we correspondingly compute volume-averaged Compton/GFL yields based on the fact that lobe sizes and projected distances (from the central galaxy) are much larger than the size of the galaxy, which we treat as a point source (Persic & Rephaeli 2019b).

Radio emission in the lobes is by electron synchrotron in disordered magnetic fields whose mean value $B$ is taken to be spatially uniform, and X-ray and $\gamma$-ray emission is by Compton scattering off the CMB and optical radiation fields. The calculations of the emissivities from these processes are standard (e.g. Persic & Rephaeli 2019a). Assuming steady state, the CRe spectrum is assumed to be spatially isotropic, truncated–power-law (PL) distribution in the electron Lorentz factor, $N_e(\gamma) = N_{e0}\,\gamma^{-q_e}$ in the interval $[\gamma_{min},\ \gamma_{max}]$. The photoelectrically absorbed ($N_{\rm H} = 1.2 \times 10^{21}$ cm$^2$; Landi et al. 2009) X-ray spectrum is used to determine $N_{e0}$ and $q_e$; alternatively, the $\gamma$-ray spectrum can be used if the GFL field is precisely known and no appreciable $\pi^0$-decay emission is assumed (as deduced in other analyses of radio lobe SEDs; Persic & Rephaeli 2019a, b, 2020). Comparison of the predicted and measured radio spectra yields $B$. The radio and $\gamma$-ray high-frequency spectral turnovers reflect the same value of $\gamma_{\rm max}$.

Before modelling the broad-band SED as outlined above, we must assess the origin of the (the soft and hard) X-ray spectrum in order to identify a Compton/CMB component. As discussed above, the *XMM* map does not show any clear extended emission (when account is taken of the detector point spread function) and because of insufficient spatial resolution of INTEGRAL/IBIS, we cannot resolve the hard X-rays emission into core and lobes. Accordingly, X-ray emission is assumed to originate from two regions: a central point-like AGN corona (and disc) and two outer extended lobes; however, emission from the lobe is estimated to be below the *XMM* sensitivity.

Therefore, a viable SED model comprises a nuclear component, modelled as a cutoff-PL with a photon index $\Gamma = 1.6$ (compatible with values in Lubiński et al. 2016), a cut-off energy $E_{\rm c} = 250$ keV, representing the AGN corona, and an extended lobe component, modelled as Compton/CMB emission.

We parametrize the relative contribution of the two components in terms of the fraction, $f$, of lobe emission at 1 keV. From the fact that emission from the lobes is not seen in the *XMM* surface brightness map, we choose a low value of $f$ of a few percent. The model overlaid on data in Fig. 6 has $f = 2.5$ per cent.[4]

The GFL provides the dominant contribution to the Comptonized starlight, whereas the EBL component is sub-dominant (similar to Fornax A; Persic & Rephaeli 2019a). We note that, in principle, the GFL contribution has no degrees of freedom once, for a given CRe spectrum, the galaxy luminosity is known: However, in this case the latter is poorly known so some freedom exists in matching the *Fermi*/LAT data. (A reliable central galaxy luminosity would clearly help in determining the CRe spectral normalization hence the lobe contribution to the X-ray emission.) Given the uncertainty on the host $V$ mag (and the LAT data, as well), a putative minor contribution from the inner jet (∼10 per cent/5 per cent at the lowest/highest energy LAT point; see previous section) can be easily accommodated in the overall SED model. A moderate level of uncertainty of just 0.1 mag fainter $V$ mag would be equivalent to this level of contribution.

Given the substantial uncertainties stemming from the lack of spatial distribution of the emission, the above SED model – which is not based on exact statistical analysis – is meant to be merely

[4]Emission parameters are: $N_{e0} = 5.9\,E - 3$ cm$^{-3}$, $q_e = 2.32$, $\gamma_{\rm min} = 100$, $\gamma_{\rm max} = 6\,E + 4$, $B = 0.65$ μG; $V = 15.86$ mag (Onken et al. 2019), $(B - V) = 0.4$ mag (typical of spiral discs which Seyfert 1 nuclei resemble).

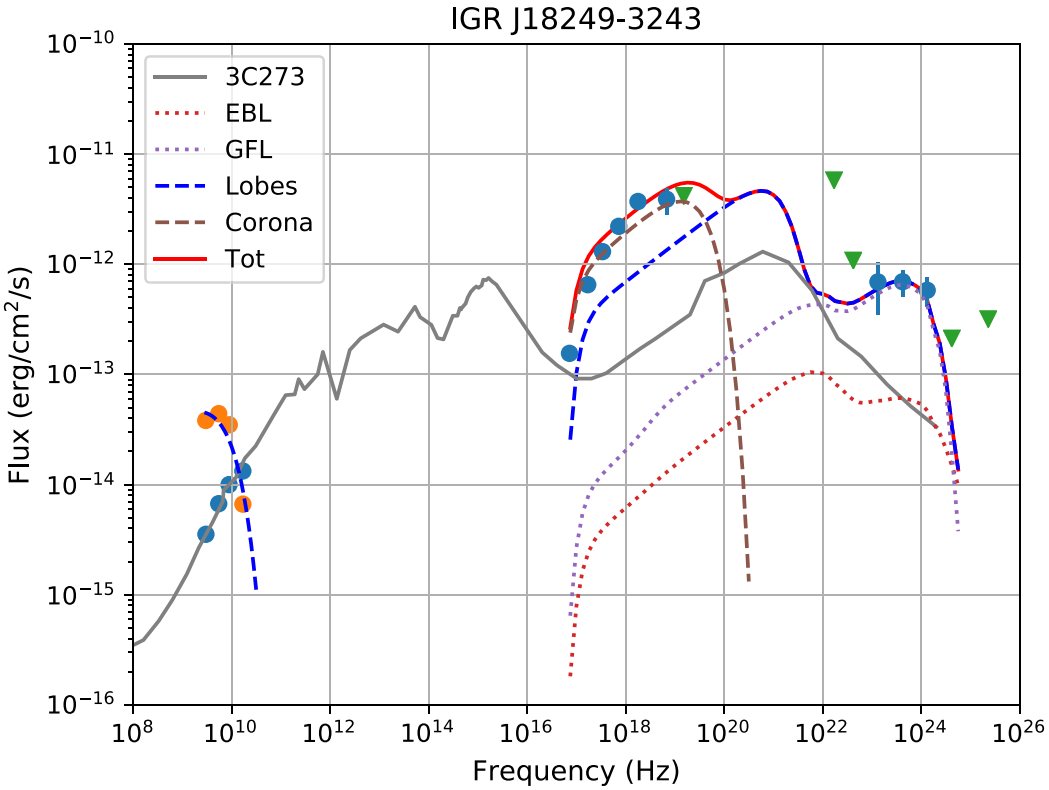


**Figure 6.** Broad band SED of IGR J18249−3243. In the radio frequencies range, orange points indicate the flux densities from the lobes, while blue dots the core ones. The grey solid line indicates the 3C 273 average spectrum from Soldi et al. (2008), normalized to the 5 GHz radio core flux density. The contribution of the different model components to the SED is indicated with dashed lines of different colours (dotted lines are the lobes sub-components due to foreground and background photon fields), while the red solid line shows the total flux density.

suggestive as to the likely origin of (most of) the observed $\gamma$-ray emission.

## 3 NEW RADIO GALAXIES AMONG *Fermi*/LAT DETECTED AGN

The discovery of yet another radio galaxy among *Fermi* detected AGN, raises the question of how many such objects are still hidden among the general population of GeV emitters, mainly due to the lack of resolution and sensitivity of classical radio surveys used so far for identification/classification purposes of *Fermi*/LAT sources. Furthermore, the fact that IGR J18249−3243 is an FR II type object queries the evidence that FR-I radio galaxies are preferentially seen among AGN emitting at high $\gamma$-ray energies (Abdo et al. 2010b). Recent radio surveys like VLASS and RACS in the GHz domain, and the LOFAR Two-metre Sky Survey (LoTSS; Shimwell et al. 2017) in the MHz domain, have provided a significant improvement both in sensitivity and resolution over previous ones, offering the opportunity to discover new radio galaxies among *Fermi*/LAT AGN. This also makes possible to reassess the ratio of FR I versus FR II types, and therefore provides more insight into the origin of the $\gamma$-ray emission in radio galaxies.

In the following, we provide observational evidence that a small sample (eight objects) of *Fermi*/LAT AGN can be classified as new radio galaxies either from the literature/available data bases or by means of our own analysis using VLASS, RACS, and LoTSS images. We note that the 'AGN' classification used in *Fermi*/LAT catalogues is defined as to exclude blazars or candidates of such class, thus already being a good indication of a possible misaligned nature of the source.

### 3.1 New GeV-emitting radio galaxies from the latest radio surveys

Recently, Chiaro et al. (2020) compiled a list of candidate Gev-emitting misaligned AGN (MAGN) by cross-correlating the fourth *Fermi*/LAT catalogue with the NVSS and SUMSS radio surveys. At the resolution and sensitivity of these surveys (HPBW $\approx$ 45 arcsec, rms $\approx$ 0.5–1.2 mJy per beam), they could identify 48 objects with an angular extension larger than the survey beam. To improve their classification, we cross-correlated their list of candidate MAGN with the latest VLASS and RACS radio surveys, in order to have higher sensitivity and resolution images. Among the objects listed by Chiaro et al. (2020) that were mapped by these recent surveys, four clearly show a resolved, double-lobed morphology in the images (see Table 3). All of them were detected in VLASS, and three out of four also in the RACS survey. We note that the initial condition adopted by Chiaro et al. (2020) for these sources to be larger than the NVSS or SUMMS HPBW selects only the largest objects, while the population of young/compact radio sources remains unexplored. Indeed, they can occasionally be $\gamma$-ray emitters (see e.g. the review by O'Dea & Saikia 2021).

The collected images are presented in Figs A1 and A2. For each source, we report the VLASS image with RACS contours superimposed (left-hand panel), and the Pan-STARRS or DSS image (right-hand panel), again with RACS contours overlaid. The latter show

**Table 3.** New radio galaxies from the latest radio surveys (top four objects) or from the literature (bottom four objects) with emission in the GeV band detected by *Fermi*/LAT. In the last two columns, we report the total flux density and radio power (for sources with known redshift) as measured at 1.4 GHz from NVSS, or at 0.8 GHz from RACS for the Southern source PKS 1234−723.

| 4FGL ID | Other ID | $z$ | Survey/Ref. | LS (arcsec) | LS (kpc) | Total flux density (mJy) | Total radio power log(W/Hz) | Class |
|---|---|---|---|---|---|---|---|---|
| J0119.6+4158 | NVSS J012002+420008 | 0.109 | VLASS/LoTSS | 110 | 216 | $255.0 \pm 8.8$ | 24.83 | FRI |
| J0929.3−2414 | NVSS J092928–241632 | – | VLASS/RACS | 130 | – | $264.9 \pm 8.9$ | – | FRI |
| J1344.4−3656 | NVSS J134423–365627 | – | VLASS/RACS | 54 | – | $508.4 \pm 17.9$ | – | FRII |
| J1455.4−3654 | NVSS J145509–365519 | 0.095 | VLASS/RACS | 210 | 365 | $1070.3 \pm 34.4$ | 25.34 | FRI |
| J0038.7−0204 | 3C 17 | 0.220 | Morganti et al. (1999) | 38 | 181 | $6187.8 \pm 239.1$ | 26.85 | FRI/II |
| J0522.9−3628 | PKS 0521–36 | 0.055 | D'Ammando et al. (2015) | 50 | 53 | $11882.9 \pm 356.5$ | 25.89 | FRI/II |
| J1236.9−7232 | PKS 1234–723 | 0.0234 | Lloyd & Jones (2002) | 840 | 391 | $1341 \pm 67$ | 24.20 | FRI |
| J2334.9−2346 | PKS 2331–240 | 0.0475 | Hernández-García et al. (2017) | 1320 | 1150 | $1141.0 \pm 57.0$ | 24.75 | FRII |

the extended lobes emission, not detected by VLASS because of the different survey design. The optical image helps in verifying that the radio core position corresponds with the host galaxy, confirming the double-lobed morphology (and thus the radio galaxy classification) for all of them. Given the declination of 4FGL J0119.6+4158, RACS data were not available. We thus made use of the LoTSS DR2 image at 150 MHz, at an angular resolution of 6 arcsec (Shimwell et al. 2022).

The optical redshift is available in the literature for two sources only. For 4FGL J1455.4−3654, Jackson et al. (2002) provide a redshift of $z = 0.095$. For 4FGL J0119.6+4158, Peña-Herazo et al. (2020) report a redshift of $z = 0.109$ and an optical classification as a BL Lac galaxy-dominated source (bzg); these objects are usually reported as BL Lac in the literature, but with an energy distribution dominated by emission from the host galaxy. However, as the authors state, not all bzg are expected to be genuine blazar as some could be moderately bright AGNs, such as radio galaxies, with non-thermal emission without strong relativistic beaming; this turns out to be the case for 4FGL J0119.6+4158/2MASX J01200274 +4200139.

The linear size and radio power are reported in Table 3, together with the suggested FR classification based on the radio power at 1.4 GHz and morphology.

### 3.2 New GeV-emitting radio galaxies from the literature

In a recent work, Angioni (2020) used the sample of radio galaxies presented in 4LAC to quantify how many FR I versus FR II types emit at $\gamma$-ray energies. He assumed as a dividing threshold between the two classes of objects a total 1.4 GHz radio power of $10^{25}$ W/Hz, finding 28 FR I and 12 FR II objects in addition to PKS 1718−649, the first young radio galaxy detected in $\gamma$-rays (Giroletti & Polatidis 2009; Migliori et al. 2016). The latter was classified by Ostorero et al. (2017) as a GigaHertz-Peaked Spectrum (GPS) source, as well as a Compact Symmetric Object (CSO). Some of the sources listed in Angioni (2020) were classified in the original *Fermi*/LAT sample as AGN, but a closer look at their morphology indicates the classical double-lobed structure. We therefore expand this previous analysis to include all objects from the Ajello et al. (2020) list that are classified as non-blazar but not included in Angioni (2020); we searched for each object the literature or available data base to confirm if the radio structure was that of a radio galaxy. As a result of this analysis, we have been able to add to the list of radio galaxies compiled by Angioni (2020) the following four objects with their relative classification:

(i) 4FGL J0038.7−0204: this radio galaxy, fully described in Morganti et al. (1999), displays a peculiar radio morphology: on the south-east side of the nucleus a very bent jet is observed while on the western side a lobe structure is visible with a ring-like shape. The 1.4 GHz radio power of $7.9 \times 10^{26}$ W/Hz is almost two orders of magnitude above the division between FR I and FR II types assumed by Angioni (2020), pointing to an FR II classification, but the ambiguous radio morphology led Miller & Brandt (2009) to define the source as another example of the 'hybrid' (FR I/FR II) radio galaxy type. The classification of this source was later changed to radio galaxy in the 4LAC update (Lott, Gasparrini & Ciprini 2020).

(ii) 4FGL J0522.9−3628: as already reported by Ajello et al. (2020), D'Ammando et al. (2015) presented a multiwaveband study of this object from radio to $\gamma$-rays – indeed, it was already present in the 3FGL catalogue by Acero et al. 2015 – highlighting its intermediate nature between broad-line radio galaxies (BLRG) and steep spectrum radio quasars (SSRQ). Its power at 1.4 GHz is $7.8 \times 10^{25}$ W/Hz, slightly larger than the threshold for the FR II class. Its morphology is not completely resolved at the resolution of the available observations, and the source is not yet included in the VLASS survey. D'Ammando et al. (2015) identified three components: the core, a jet-like structure towards NW, and a further component towards SE. Their broad-band SED fitting suggests a viewing angle between 6 and 15 deg.

(iii) 4FGL J1236.9−7232: this source is fully discussed by Lloyd & Jones (2002) and classified as an FR I on the basis of ATCA images. This is also confirmed by its radio power at 1.4 GHz of $1.58 \times 10^{24}$ W/Hz, calculated from the flux density reported in the NVSS catalogue. Finally, its noticeable angular size of 14 arcmin translates into a projected linear size of 391 kpc. Also, the source classification is now radio galaxy in the 4LAC update (Lott et al. 2020).

(iv) 4FGL J2334.9−23469: as pointed out by Ajello et al. (2020), this sources was fully analysed by Hernández-García et al. (2017, 2018) and found to host a blazar-like nucleus in a giant size radio galaxy (1.2 Mpc) displaying an FR II morphology; to reconcile these two opposite observational pieces of evidence, the authors suggest that the source suffered a dramatic change in jet orientation as a consequence of restarting activity. The total power at 1.4 GHz is $5.62 \times 10^{24}$ W/Hz, slightly below the limit for FR I/FR II classification. Given the peculiar nature of this source, and the suspected reactivation and reorientation of the core, the emission detected by *Fermi*/LAT could be due to the blazar corresponding with its core, that would then pertain to the blazar class rather than to the radio galaxies one.

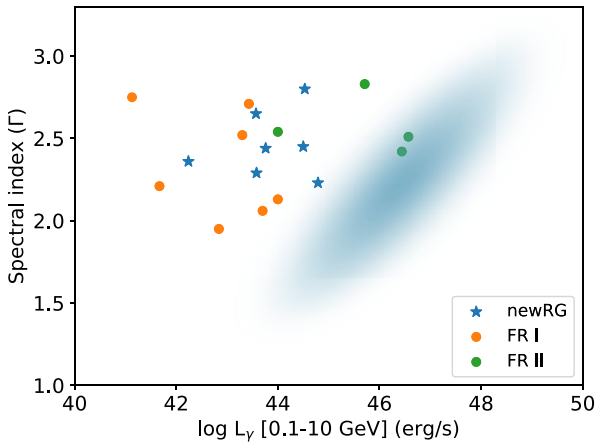


**Figure 7.** Spectral index at GeV energies (Γ) as a function of the 0.1–10 GeV luminosity. The locus of blazars is indicated as a shaded area. FR I and FR II from Abdo et al. (2010b) are in orange and green points, respectively, while the newly discovered radio galaxies with a redshift estimate are represented as blue stars.

### 3.3 Main properties

We used data from the latest radio surveys and information in the literature to identify further radio galaxies among *Fermi*/LAT AGN. In total we found nine such objects, including IGR J18249−3243 that has been the main focus of this paper: four can be confidently classified as FR I while two as FR II and other two as intermediate FR I/FR II objects. This allows to update the relative abundance of FR I and FR II among GeV emitting radio galaxies. Expanding on the list of Angioni (2020), we find an FR I versus FR II ratio of roughly 2.5 (32 FR I versus 14 FR II plus two intermediate sources), thus confirming the prevalence of FR I radio galaxies initially found by Abdo et al. (2010b), and not yet fully explained in the literature.

Among the five newly discovered radio galaxies found in VLASS (IGR J18249−3243 plus bottom half of Table 3), three have an estimate of the redshift value, making possible the calculation of the $\gamma$-ray luminosity from 4FGL flux values. In addition to these ones, we consider also the four objects found in the literature. We then used the Γ versus log L$_\gamma$ [0.1–10 GeV] (erg s$^{-1}$) diagram (see Fig. 7) to display our seven sources in comparison with the 11 MAGNs detected by *Fermi*/LAT in the first 15 months of observations and discussed by Abdo et al. (2010b); also shown in the figure is the locus of blazar-like objects. The sample of 11 objects included seven FR I and four FR II radio galaxies. The latter showed $\gamma$-ray luminosities similar to blazars, while the FR I ones were typically three orders of magnitude lower. It is evident from the figure that our radio galaxies display lower $\gamma$-ray luminosities than blazar-like objects; in addition we note that our objects have intermediate values compared to previously known radio galaxies.

Abdo et al. (2010b) also estimated the core dominance of MAGNs, proxy of their orientation, finding high values when compared with the 3CRR sample. This indicates a preferred orientation along the jet axis for *Fermi*/LAT MAGNs. Regarding our objects, we used VLASS images to estimate the core dominance at 3 GHz for the five objects discovered from VLASS with this work (top half of Table 4), while we compiled values from the literature for the others (bottom half of Table 4). The collected values range from ∼0.1 to ∼1.5.

Overall, we conclude that the new GeV emitting radio galaxies found in this work have core dominance values within the range reported by Abdo et al. (2010b), suggesting the same preferred polar orientation for MAGNs.

**Table 4.** Collected quantities for the new *Fermi*/LAT radio galaxies from VLASS (top half) or the literature (bottom half), used for the comparison with Abdo et al. (2010b).

| 4FGL ID | CD | log L$_\gamma$ [0.1–10 GeV] (erg s$^{-1}$) | Γ |
|---|---|---|---|
| J0119.6+4158 | 0.29 | 43.58 | 2.29 ± 0.16 |
| J0929.3−2414 | 0.89 | – | 2.22 ± 0.16 |
| J1344.4−3656 | 0.24 | – | 2.30 ± 0.11 |
| J1455.4−3654 | 1.45 | 43.76 | 2.44 ± 0.14 |
| J1824.7−3243 | 0.09 | 44.79 | 2.23 ± 0.12 |
| J0038.7−0204 | 0.33 | 44.53 | 2.80 ± 0.11 |
| J0522.9−3628 | 0.79 | 44.50 | 2.45 ± 0.01 |
| J1236.9−7232 | 1.49 | 42.24 | 2.36 ± 0.12 |
| J2334.9−2346 | 0.45 | 43.57 | 2.65 ± 0.14 |

## 4 FINAL REMARKS

### 4.1 The emerging population of GeV-emitting radio galaxies

In this work, we presented pieces of evidence of how IGR J18249−3243, reported as a new detection in the *Fermi*/LAT survey of Ajello et al. (2020) and generically classified as an AGN, is actually a radio galaxy of the FR II type. Its double-lobed structure was missed until now due to the lack of resolution in classical radio surveys such as NVSS and SUMSS. The discovery that IGR 18249−3243 is a radio galaxy of the FR II type raises further considerations, in terms of the incidence of $\gamma$-ray emission on the general AGN population, and more specifically in radio galaxies. Considering our broad-band SED modelling of IGR J18249−3243, and its possible GeV emission from the lobes, we can foresee that more FR II objects with a GeV counterpart will emerge from new, deeper, and sharper radio surveys, softening the prevalence of FR I found so far (Abdo et al. 2010b). A first example of the potentiality of these surveys has been provided in Section 3.1, where we could identify four new radio galaxies among the 47 candidates (∼10 per cent) provided by Chiaro et al. (2020).

As new censuses of $\gamma$-ray sources are built, an emerging population of MAGNs and non-blazar sources is being found (Foschini et al. 2021). In particular, the recently introduced class of FR0 sources (Baldi, Capetti & Giovannini 2015), constituting the low-luminosity bulk of the radio emitting AGN population, are thought to give a contribution of up to ∼20 per cent to the unresolved $\gamma$-ray background (Stecker, Shrader & Malkan 2019; Paliya 2021). In addition, recent *Fermi*/LAT studies on the population of young radio sources (Principe et al. 2020, 2021) found that some individual objects can be bright $\gamma$-ray sources, although the population as a whole seems to lie below the *Fermi*/LAT detection threshold. The compact nature of these sources will be better investigated with future radio surveys, as well as with future higher resolution $\gamma$-ray observatories, possibly revealing a larger population of radio galaxies emitting at GeV energies.

### 4.2 GeV emission in the *INTEGRAL* hard X-ray AGN sample

IGR J18249−3243 is included in the *INTEGRAL* complete sample of AGN (Malizia et al. 2012), which is now fully covered by *Fermi*/LAT

observations, providing an idea on the role of $\gamma$-ray emission in local hard X-ray bright AGN. In particular, if compared to the latest *Fermi* 10 yr catalogue, this sample can give an estimate of how many local AGN emit strongly above 100–200 keV, reaching the GeV band. The sample was extracted from the third *INTEGRAL*/IBIS survey to study the distribution of the absorption in the local Universe (Malizia et al. 2012). It consists of 87 objects [5] divided in 46 type 1 (Seyfert 1-1.5, of which 5 Narrow Line Seyfert 1) and 33 type 2 (Seyfert 1.8-2) AGN; only 8 blazars (BLLac-QSO) were reported in the catalogue. All of these eight blazars have emission in the MeV/GeV band, confirming that despite being rare they belong to the main contributing class at high energies. Another object with GeV detection in this complete INTEGRAL sample of AGN (IGR J13109−5552) is classified as a blazar candidate of uncertain type; in order to define its true nature we obtained ATCA radio observations and also analysed measurements available in the literature: as a consequence we have been able to classify the source as a true blazar of the Flat Spectrum Radio Quasar type (see Appendix B). This emphasized once more that hard X-ray emitting blazars emit up to the GeV domain.

Among the Seyfert population, radio galaxies with the typical double-lobed morphology are also GeV emitters: before this work, four objects (NGC 1275, B3 0309+411B, 3C 111, and Cen A) belonging to the sample were known to be detected by *Fermi*/LAT. With the identification of IGR J18249−3243 as a new radio galaxy, we bring the above number to five.

Finally, three Seyferts of type 2 (Circinus, NGC 1068, and NGC 4945) have also been detected at GeV energies: interestingly all of them are Compton thick objects (i.e. heavily absorbed), but their $\gamma$-ray emission is probably associated with strong starburst activity in their host galaxy.

Overall, the $\gamma$-ray detection rate within the INTEGRAL complete sample of AGN is 20±5%, emphasizing the fact that in the majority of local active galaxies (80%) the primary continuum drops off exponentially above a few hundred keV. Besides blazars, the only other exceptions are radio jetted AGN and possibly objects with strong starburst activity. Through this work we also found that, out of 11 radio galaxies present in the INTEGRAL sample, 5 (or 45%) have a detection in the *Fermi* 10th year catalogue; the next step will be to understand what makes these five objects peculiar with respect to the other six which do not display GeV emission.

## 5 CONCLUSIONS

We can summarize our findings as follows:

(i) Thanks to the recent release of the first epoch of the VLASS survey, we identified a new *INTEGRAL*/IBIS FR II radio galaxy with detection at GeV energies by *Fermi*/LAT. We integrated the information from VLASS with further data from our ATCA campaign at 5.5, 9, and 17 GHz, and with the image from the RACS survey.

(ii) Based on broad-band SED modelling, we found that jet contribution is not sufficient to reproduce the GeV emission. Instead, we showed how it could be accounted for when considering the emission of lobes, and in particular the inverse Compton component from radio-emitting electron off ambient photon fields. This result stresses the contribution of broad-band SED modelling in characterizing the different emission regions and mechanisms, overcoming the lack of resolution at high energies.

[5] One source, IGR J03184−0014, is not considered here as it was never seen again in subsequent INTEGRAL surveys

(iii) Thanks to data from the new generation radio surveys VLASS, RACS, and LoTSS, we present a list of four newly discovered radio galaxies detected by *Fermi*/LAT. Additional four sources were compiled from the literature, for a total of eight objects. Despite their smaller projected linear size, their overall $\gamma$-ray properties are similar to the ones of previously known similar objects, suggesting the same preferred polar orientation.

(iv) We foresee that further GeV emitting radio galaxies will be found thanks to new radio surveys, providing a deeper and sharper view on the counterparts of the GeV sky. This will unveil an emerging population of radio galaxies, in addition to the larger population of blazars commonly found, making possible the study of $\gamma$-ray emission from their extended regions as done in this paper for the lobes of IGR J18249−3243.

## ACKNOWLEDGEMENTS

The authors acknowledge financial support from ASI under contract n. 2019-35-HH.0, in particular for G.B. research contract. The Australia Telescope Compact Array is part of the Australia Telescope National Facility (grid.421683.a) which is funded by the Australian Government for operation as a National Facility managed by CSIRO. The National Radio Astronomy Observatory is a facility of the National Science Foundation operated under cooperative agreement by Associated Universities, Inc. CIRADA is funded by a grant from the Canada Foundation for Innovation 2017 Innovation Fund (Project 35999), as well as by the Provinces of Ontario, British Columbia, Alberta, Manitoba and Quebec. The Pan-STARRS1 Surveys (PS1) and the PS1 public science archive have been made possible through contributions by the Institute for Astronomy, the University of Hawaii, the Pan-STARRS Project Office, the Max Planck Society and its participating institutes, the Max Planck Institute for Astronomy, Heidelberg and the Max Planck Institute for Extraterrestrial Physics, Garching, the Johns Hopkins University, Durham University, the University of Edinburgh, the-Queen's University Belfast, the Harvard-Smithsonian Center for Astrophysics, the Las Cumbres Observatory Global Telescope Network Incorporated, the National Central University of Taiwan, the Space Telescope Science Institute, the National Aeronautics and Space Administration under Grant No. NNX08AR22G issued through the Planetary Science Division of the NASA Science Mission Directorate, the National Science Foundation Grant No. AST-1238877,the University of Maryland, Eotvos Lorand University (ELTE), the Los Alamos National Laboratory, and the Gordon and Betty Moore Foundation. This research has made use of the VizieR catalogue access tool, CDS, Strasbourg, France (DOI: 10.26093/cds/vizier). LOFAR data products were provided by the LOFAR Surveys Key Science project (LSKSP; https://lofar-surveys.org/) and were derived from observations with the International LOFAR Telescope (ILT). LOFAR (van Haarlem et al. 2013) is the Low Frequency Array designed and constructed by ASTRON. It has observing, data processing, and data storage facilities in several countries, which are owned by various parties (each with their own funding sources), and which are collectively operated by the ILT foundation under a joint scientific policy. The efforts of the LSKSP have benefited from funding from the European Research Council, NOVA, NWO, CNRS-INSU, the SURF Co-operative, the UK Science and Technology Funding Council and the Jülich Supercomputing Centre.

## DATA AVAILABILITY

Most of data presented in this work are public and available from relevant archives. Those not yet public will be made available from the corresponding author upon request.

## REFERENCES


Abdo A. A. et al., 2010a, Science, 328, 725
Abdo A. A. et al., 2010b, ApJ, 720, 912
Abdollahi S. et al., 2020, ApJS, 247, 33
Acero F. et al., 2015, ApJS, 218, 23
Ackermann M. et al., 2011, ApJ, 741, 30
Ackermann M. et al., 2016, ApJ, 826, 1
Ajello M. et al., 2020, ApJ, 892, 105
Angioni R., 2020, Astropart. Phys., 116, 102393
Baldi R. D., Capetti A., Giovannini G., 2015, A&A, 576, A38
Bassani L., Venturi T., Molina M., Malizia A., Dallacasa D., Panessa F., Bazzano A., Ubertini P., 2016, MNRAS, 461, 3165
Bird A. J. et al., 2007, ApJS, 170, 175
Bird A. J. et al., 2016, ApJS, 223, 15
Buzzoni A., Arnaboldi M., Corradi R. L. M., 2006, MNRAS, 368, 877
Chiaro G., La Mura G., Domínguez A., Bisogni S., 2020, J. High Energy Astrophys., 27, 77
Condon J. J., Cotton W. D., Greisen E. W., Yin Q. F., Perley R. A., Taylor G. B., Broderick J. J., 1998, AJ, 115, 1693
Cotton W. D. et al., 2020, MNRAS, 495, 1271
D'Ammando F. et al., 2015, MNRAS, 450, 3975
Foschini L. et al., 2021, Universe, 7, 372
Franceschini A., Rodighiero G., 2017, A&A, 603, A34
Giroletti M., Polatidis A., 2009, Astron. Nachr., 330, 193
Grandi P., Palumbo G. G. C., 2007, ApJ, 659, 235
Grandi P., Torresi E., Stanghellini C., 2012, ApJ, 751, L3
Griffith M. R., Wright A. E., 1993, AJ, 105, 1666
Hernández-García L. et al., 2017, A&A, 603, A131
Hernández-García L. et al., 2018, MNRAS, 478, 4634
Intema H. T., Jagannathan P., Mooley K. P., Frail D. A., 2017, A&A, 598, A78
Jackson C. A., Wall J. V., Shaver P. A., Kellermann K. I., Hook I. M., Hawkins M. R. S., 2002, A&A, 386, 97
Kataoka J. et al., 2011, ApJ, 740, 29
Lacy M. et al., 2020, PASP, 132, 035001
Landi R. et al., 2007, Astron. Telegram, 1273, 1
Landi R. et al., 2009, A&A, 493, 893
Lloyd B. D., Jones P. A., 2002, MNRAS, 331, 717
Lott B., Gasparrini D., Ciprini S., 2020, preprint (arXiv:2010.08406)
Lubiński P. et al., 2016, MNRAS, 458, 2454
McConnell D. et al., 2020, Publ. Astron. Soc. Aust., 37, e048
McKinley B. et al., 2015, MNRAS, 446, 3478
Malizia A. et al., 2007, ApJ, 668, 81
Malizia A., Stephen J. B., Bassani L., Bird A. J., Panessa F., Ubertini P., 2009, MNRAS, 399, 944
Malizia A., Bassani L., Bazzano A., Bird A. J., Masetti N., Panessa F., Stephen J. B., Ubertini P., 2012, MNRAS, 426, 1750
Malizia A., Molina M., Bassani L., Stephen J. B., Bazzano A., Ubertini P., Bird A. J., 2014, ApJ, 782, L25
Masetti N. et al., 2008, A&A, 482, 113
Masetti N. et al., 2009, A&A, 495, 121
Migliori G., Siemiginowska A., Sobolewska M., Loh A., Corbel S., Ostorero L., Stawarz Ł., 2016, ApJ, 821, L31
Miller B. P., Brandt W. N., 2009, ApJ, 695, 755
Morganti R., Oosterloo T., Tadhunter C. N., Aiudi R., Jones P., Villar-Martin M., 1999, A&AS, 140, 355
O'Dea C. P., Saikia D. J., 2021, A&A Rev., 29, 3
Onken C. A. et al., 2019, Publ. Astron. Soc. Aust., 36, e033
Ostorero L., Morganti R., Diaferio A., Siemiginowska A., Stawarz Ł., Moderski R., Labiano A., 2017, ApJ, 849, 34
Paliya V. S., 2021, ApJ, 918, L39
Paliya V. S. et al., 2019, ApJ, 881, 154
Peña-Herazo H. A. et al., 2020, A&A, 643, A103
Persic M., Rephaeli Y., 2007, A&A, 463, 481
Persic M., Rephaeli Y., 2019a, MNRAS, 485, 2001
Persic M., Rephaeli Y., 2019b, MNRAS, 490, 1489
Persic M., Rephaeli Y., 2020, MNRAS, 491, 5740
Prieto M. A., Reunanen J., Tristram K. R. W., Neumayer N., Fernandez-Ontiveros J. A., Orienti M., Meisenheimer K., 2010, MNRAS, 402, 724
Principe G. et al., 2020, A&A, 635, A185
Principe G., Di Venere L., Orienti M., Migliori G., D'Ammando F., Mazziotta M. N., Giroletti M., 2021, MNRAS, 507, 4564
Ricci C. et al., 2017, ApJS, 233, 17
Shimwell T. W. et al., 2017, A&A, 598, A104
Shimwell T. W. et al., 2022, A&A, 659, A1
Soldi S. et al., 2008, A&A, 486, 411
Stecker F. W., Shrader C. R., Malkan M. A., 2019, ApJ, 879, 68
Torresi E., Grandi P., Capetti A., Baldi R. D., Giovannini G., 2018, MNRAS, 476, 5535
Trinchieri G., Wolter A., and Iovino A., 1998, in Breitschwerdt D.,Freiberg M.-J., Truemper J., eds, IAU Colloq. 166: The Local Bubble and Beyond. Vol. 506, A Ring of X-rays from the Cartwheel Galaxy, Springer-Verlag, Berlin Heidelberg New York, p. 551
Wayth R. B. et al., 2015, Publ. Astron. Soc. Aust., 32, e025
Wozniak P. R., Zdziarski A. A., Smith D., Madejski G. M., Johnson W. N., 1998, MNRAS, 299, 449


## APPENDIX A: IMAGES OF NEWLY DISCOVERED GEV RADIO GALAXIES

Here, we report the images (Figs A1 and A2) of the newly discovered radio galaxies from the latest radio surveys, discussed in Section 3.1. For each source we report the VLASS radio image with RACS or LoTSS DR2 contours superimposed, and the overlay of radio contours on the optical image from Pan-STARRS or DSS2. The beam is reported in the lower left corner. Contours are multiples of 3 × rms, namely −1, 1, 2, 4, 8, 16, 32, 64, 128, 256. For sources 4FGL J0929.3−2414 and 4FGL J1455.4−3654 contours start from 12-× rms, due to presence of image artefacts.

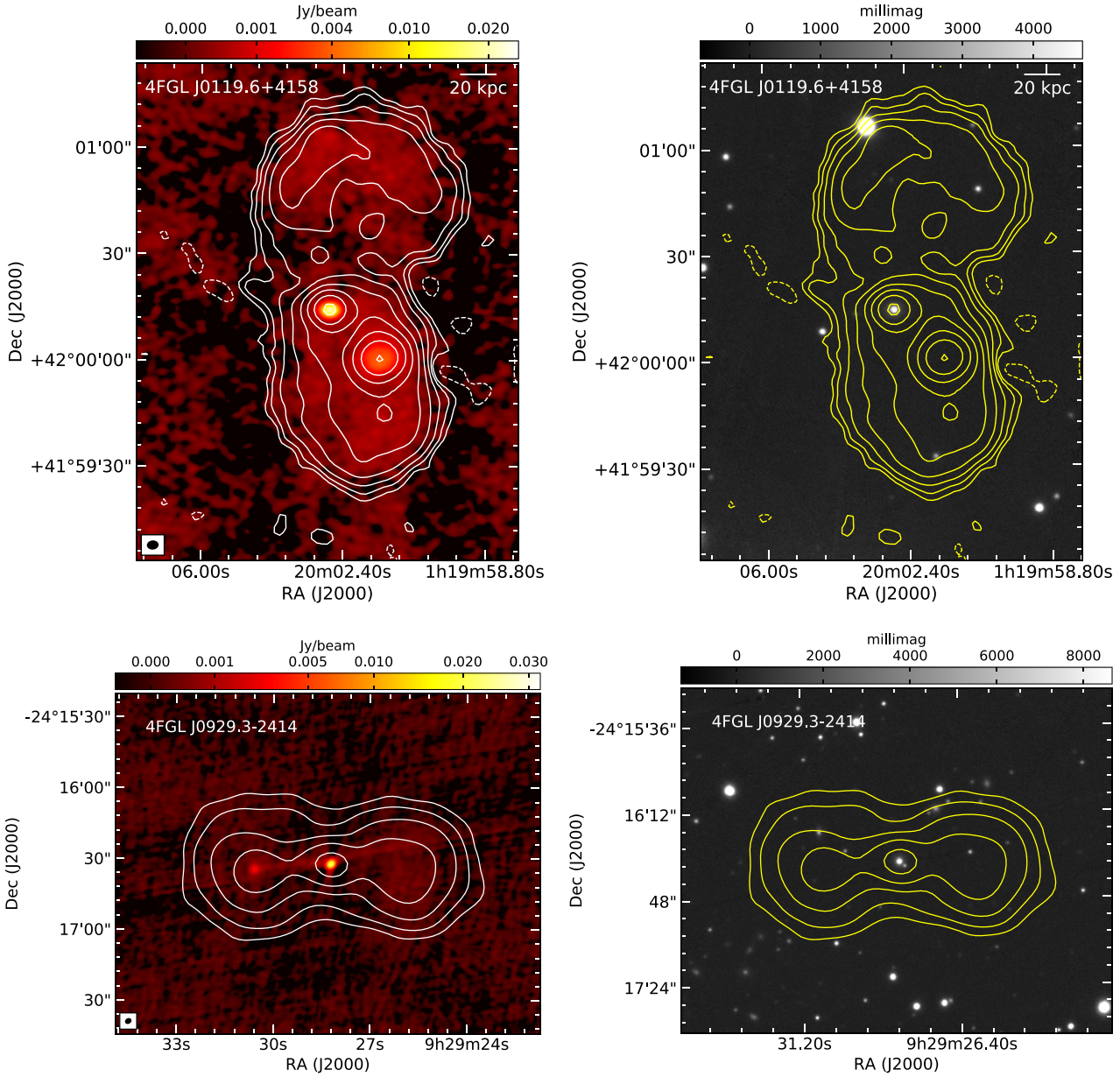


**Figure A1.** Images of newly discovered radio galaxies from recent surveys. Top panels: VLASS (3 GHz) image of source 4FGL J0119.6+4158 with LoTSS (150 MHz) contours superimposed (left) and Pan-STARRS image with LoTSS DR2 contours superimposed (right). Bottom panels: VLASS image of source 4FGL J0929.3−2414 with RACS (0.88 GHz) contours superimposed (left) and Pan-STARRS image with RACS contours superimposed (right).

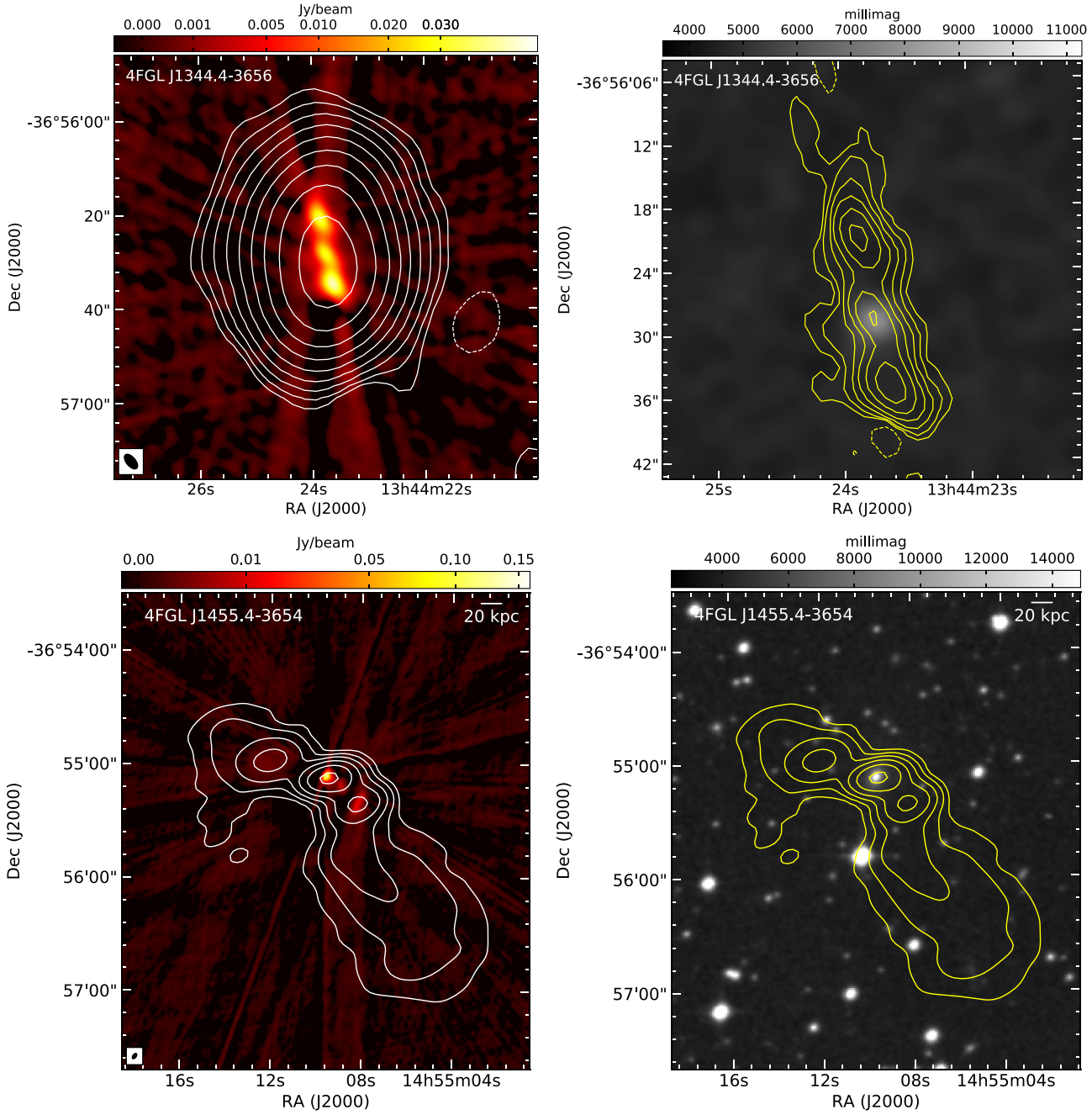


**Figure A2.** Same as for Fig. A1, but for sources 4FGL J1344.4−3656 and 4FGL J1455.4−3654. Top left panel is VLASS image with RACS contours superimposed, top right panel is the DSS2 image with VLASS contours superimposed. Bottom left panel is VLASS image with RACS contours, while bottom right panel DSS2 image with RACS contours.

## APPENDIX B: THE BLAZAR IGR J13109−5552

This source was first reported by *INTEGRAL*/IBIS as part of the third survey catalogue (Bird et al. 2007). Shortly after, Malizia et al. (2007) provided the location of the X-ray counterpart by means of *Swift*/XRT follow-up observations. The X-ray position at RA(J2000) = 13:10:43.08, Dec(J2000) = –55:52:11.66 (positional uncertainty of 3.7 arcsec) allowed to match the source with a strong radio emitter (PMN J1310−5552). Furthermore, the restricted X-ray error circle enabled the identification of the optical counterpart, and through follow-up spectroscopic observations a loose [6] classification of the source: IGR J13109−5552 is a type 1 AGN at a redshift of 0.104 (Masetti et al. 2008). The source black hole mass is $2 \times 10^8$ solar masses (Paliya et al. 2019).

The combined *XMM*/pn plus *INTEGRAL*/IBIS, and *Swift*/XRT plus *Swift*/BAT spectra, also presented by Malizia et al. (2014), can be described by a simple power law ($\Gamma$=1.4-1.5) with no evidence

[6]This is due to an anomalous optical spectrum, possibly caused by an intervening object. See Masetti et al. (2008) for more details

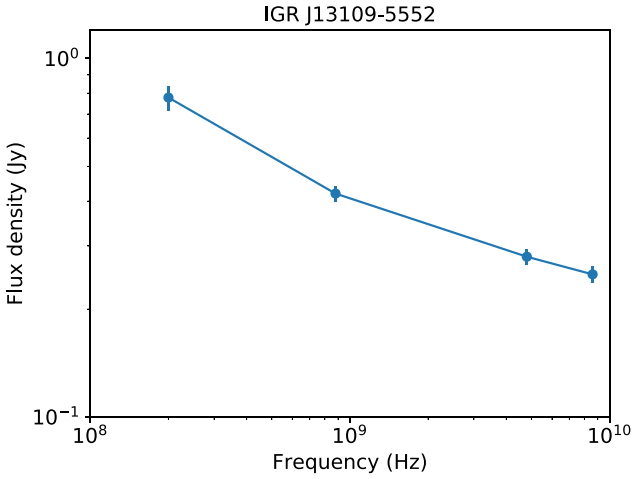


**Figure B1.** Radio SED for IGR J13109−5552 built with GLEAM (0.2 GHz), RACS (0.88 GHz), and ATCA data from our campaign (4.8, 8.6 GHz).

**Table B1.** Collected radio flux densities for IGR J13109−5552.

| Telescope | Frequency (GHz) | Rms (mJy per beam) | Flux density (mJy) |
|---|---|---|---|
| GLEAM | 0.2 | 37 | $778 \pm 60$ |
| RACS | 0.88 | 0.25 | $420 \pm 21$ |
| ATCA | 4.8 | 2.19 | $280 \pm 14$ |
| ATCA | 8.6 | 3.89 | $250 \pm 13$ |

of a high-energy cut-off ($E_{\rm cut} > 360$ keV; Malizia et al. 2014) nor of reflection (Ricci et al. 2017). The source is reported as persistent in the latest IBIS catalogue (Bird et al. 2016). In a recent analysis of beamed AGN detected by *Swift*/BAT and *Fermi*/LAT (Paliya et al. 2019), it was classified as a blazar candidate of uncertain type due to its SED and radio detection. The source SED is indeed characterized by two broad peaks as observed in blazars, but that can also be found in some misaligned AGN.

At radio wavelengths, IGR J13109−5552 is included in the most recent surveys of the Southern emisphere: GLEAM and RACS. In addition, we observed this source during the ATCA run described in Section 2.1.1, providing further two images at 4.8 and 8.6 GHz. The source results unresolved down to an angular resolution of 2.0 arcsec × 0.6 arcsec, provided by our highest resolution ATCA observations. At the redshift of the source, this translates into a projected linear size smaller than ∼1 kpc. This allows us to combine data from surveys and observations at different resolutions to build the radio SED of this object. The collected flux densities are given in Table B1, while the corresponding radio SED in Fig. B1. The spectral index is flat from low to high frequencies, ranging from $-0.42 \pm 0.06$ (0.2–0.88 GHz) to $-0.19 \pm 0.12$ (4.8–8.6 GHz. As a whole, the unresolved morphology and the flat radio spectrum support the classification as blazar, and in particular as a flat-spectrum radio quasar.

Finally, the *Fermi* $\gamma$-ray spectrum is described by a simple power law with photon index $2.759 \pm 0.135$ and a 0.1–100 GeV flux of $7.42 \pm 1.39 \times 10^{-12}$ erg cm$^{-2}$ s$^{-1}$ (Ajello et al. 2020). At the source redshift, this implies a $\gamma$-ray luminosity of $2 \times 10^{44}$ erg s$^{-1}$: this luminosity is one of the lowest among *Fermi* flat spectrum radio quasars reported in Ajello et al. (2020). Moreover, the source is reported as variable in the 4FGL catalogue, having a variability index of 74.5, further supporting the blazar classification.

This paper has been typeset from a TEX/LATEX file prepared by the author.